Topological diffusive metal in amorphous transition metal mono-silicides

Selma Franca, Adolfo G. Grushin

Topological diffusive metal in amorphous transition metal mono-silicides

Selma Franca[1,*] and Adolfo G. Grushin[1,†]

[1] *Univ. Grenoble Alpes, CNRS, Grenoble INP, Institut Néel, 38000 Grenoble, France*

(Dated: June 30, 2023)

In chiral crystals crystalline symmetries can protect multifold fermions, pseudo-relativistic masless quasiparticles that have no high-energy counterparts. Their realization in transition metal mono-silicides has exemplified their intriguing physical properties, such as long Fermi arc surface states and unusual optical responses. Recent experimental studies on amorphous transition metal mono-silicides suggest that topological properties may survive beyond crystals, even though theoretical evidence is lacking. Motivated by these findings, we theoretically study a tight-binding model of amorphous transition metal mono-silicides. We find that topological properties of multifold fermions survive in the presence of structural disorder that converts the semimetal into a diffusive metal. We characterize this topological diffusive metal phase with the spectral localizer, a real-space topological indicator that we show can signal multifold fermions. Our findings showcase how topological properties can survive in disordered metals, and how they can be uncovered using the spectral localizer.

Introduction — Crystalline topological metals host quasiparticles classified according to the symmetries required to protect them. For example, Weyl semimetals require no symmetries to realize Weyl quasiparticles, which are spin-half, gapless low-energy quasiparticles governed by the Weyl equation [1]. Weyl bands disperse linearly around a two-band crossing point, accompanied by a quantized flux of Berry curvature, known as the monopole charge. The absence of symmetry requirements endows Weyl points with a relative robustness against disorder [2–20], explaining why they have been predicted to survive even in non-crystalline lattices [21].

Higher-spin generalizations of Weyl quasiparticles known as multifold fermions, predicted and observed in chiral crystals [22–31], seem more delicate. Their bands disperse linearly around a multi-band crossing points and can have an associated monopole charge. However, in contrast to Weyl quasiparticles, they require crystalline symmetries to ensure their robustness. The effect of disorder on multifold semimetals is much less explored [32, 33], and it seems paradoxical that topology can survive the absence of long-range lattice order.

In this work we investigate to what extent the above expectation holds in a non-crystalline amorphous model. Our main result is that topological properties of multifold fermions can survive the absence of crystal symmetry. Recently, amorphous insulators have been predicted and observed to display topological phases, owing to the finite energy scale endowed by the gap [34–47]. Indeed, models of amorphous Chern insulators [34–36, 38–40], quantum spin-Hall insulators [41–44] and 3D topological insulators [34, 45, 46], demonstrate that topology survives the amorphicity, and can even be induced by it [43]. Moreover, average crystalline symmetries can also protect amorphous topological states, provided that the disorder strength is smaller than the band gap [48–52].

In turn, the survival of topology in amorphous metals is much more challenging to address due to the absence of a gap. Methods to detect metallic topology in real-space are scarce, especially in the presence of time-reversal symmetry where local Chern markers [53, 54] are identically zero.

To make progress, here we amorphisize a known crystalline model of a chiral crystal in space group 198 [24, 27, 55, 56]. Materials in this space group, such as the transition metal mono-silicides RhSi or CoSi, lack inversion and mirror symmetries yet exhibit nonsymmorphic symmetries. These materials manifest exotic physical properties such as multifold fermions at the Fermi level, long Fermi arcs surface states [55], a quantized circular photogalvanic effect [31, 55, 57–60] and unusual magneto-transport features [23, 55, 61, 62]. Moreover, a recent experimental study on amorphous CoSi (a-CoSi) has found a range of intriguing magneto-transport properties [63].

Using the recently introduced spectral localizer [64–69], we find that multifold fermions enter a topological diffusive phase in the presence of moderate structural disorder. We find that localizer in-gap modes can be traced back to the existence of multifold fermions and coexisting with spectral properties characteristic of a diffusive metal [13]. Upon increasing disorder, the localizer in-gap modes are lost, leaving behind a trivial diffusive metal that eventually localizes into a trivial Anderson insulator. Using the spectral localizer to define topological diffusive metals can be extended to any symmetry class, and hence is the main result of this work (see Fig. 1a).

Model Hamiltonian — Amorphous systems lack long-range order, but they display short-range ordering, dictated by the local chemistry of the elements [70]. This implies the existence of preferred bond lengths and angles peaked around the crystalline values [71–73]. Hence, we first revisit the crystalline model of RhSi and CoSi, in space group 198, on which we base our amorphous model. This space group has three non-intersecting twofold screw symmetries $s_{2x,y,z}$ and a diagonal cubic threefold rotation $C_{3,111}$. The spin-orbit coupling in RhSi [55] and

CoSi [74] is weak (tens of meV), and is neglected in our simulations. In this case, the band-structure near the Fermi level is captured by a tight-binding Hamiltonian with four s-type orbitals (A, B, C, D) positioned at $(0,0,0),(\frac{a}{2},0,\frac{a}{2}),(\frac{a}{2},\frac{a}{2},0)$ and $(0,\frac{a}{2},\frac{a}{2})$, see Fig. 1b [55]. In the following, we measure all distances in units of a. Nearest-neighboring orbitals are connected by inter-orbital hoppings while second nearest-neighbors are connected via intra-orbital hoppings. Fig. 1c, illustrates the inter-orbital hoppings within the unit cell, which take two values $(v_1 \pm v_p)/4$, depending on the bond orientation. The amplitude $v_2/2$ of intra-orbital hoppings is independent of the bond orientation. The Bloch Hamiltonian is discussed further in the Supp. Mat. (SM) [75].

It is convenient to consider two parameter regimes, expressed in eV: (1) when only $v_p = -0.762$ is non-zero, and (2) when $v_1 = 0.55, v_2 = 0.16, v_p = -0.762$ eV. The hopping amplitudes in regime (2) are chosen such that the crystalline tight-binding Hamiltonian [75] reproduces well the density-functional theory calculated band-structure of RhSi near the Fermi level [55]. Hence, in the following we refer to regime (2) as a-RhSi regime. The red curves in Figs. 1d,e show bulk spectra for the two regimes, respectively. In regime (1), the spectrum is doubly degenerate in the entire Brillouin zone and features two double-Weyl fermions, one at Γ and one at the R point, occurring at the same energy $E = 0$. In the a-RhSi regime, v_1, v_2 turn the double-Weyl at Γ into a threefold fermion, energetically shifted with respect to the double-Weyl fermion at the R point. In both regimes, the crossings at Γ and R have monopole charges $C = 2$, and -2, respectively.

We create the amorphous lattice by displacing every site n (representing a single orbital) of crystalline RhSi by $\delta\mathbf{r}_n = (\delta x_n, \delta y_n, \delta z_n)$ drawn from a Gaussian distribution

$$D(\delta\mathbf{r}_n) = \frac{1}{2\pi\sigma^2}\exp\left[-\frac{|\delta\mathbf{r}_n|^2}{2\sigma^2}\right]. \quad (1)$$

The variance σ^2 is typically proportional to the quenching temperature to form the amorphous solid, $\sigma^2 \propto k_B T$ [43]. To avoid artificial clustering of sites, we impose a minimal distance of $d_{\min} = 0.4$ [48]. The possible hoppings $\tilde{v}_\alpha$ $(\alpha = 1, 2, p)$ between sites at positions $\mathbf{r}^i = (x^i, y^i, z^i)$ and $\mathbf{r}^f = (x^f, y^f, z^f)$ are determined from

$$\tilde{v}_\alpha = \tilde{v}_\alpha(d)\tilde{v}_\alpha(\theta,\phi)\exp\left[1 - \frac{d}{d_\alpha^0}\right]\Theta(d_c - d), \quad (2)$$

in spherical coordinates (d, θ, ϕ) with $d = |\mathbf{r}_f - \mathbf{r}_i|$. Here, d_α^0 depends on whether the hopping is inter-orbital, where $d_1^0 = d_p^0 = 1/\sqrt{2}$, or intra-orbital, where $d_2^0 = 1$.

Since the intra-orbital hopping $v_2/2$ of crystalline RhSi is independent of bond orientation [75], we take $\tilde{v}_2(\theta,\phi) = 1$ and $\tilde{v}_2(d) = v_2/d$. The inter-orbital hopping of crystalline RhSi has amplitudes $(v_1 \pm v_p)/4$, see Fig. 1c, where the hopping v_p is direction dependent, unlike v_1. Hence, we take $\tilde{v}_1(\theta,\phi) = 1$, $\tilde{v}_1(d) = v_1/\sqrt{2}d$ and

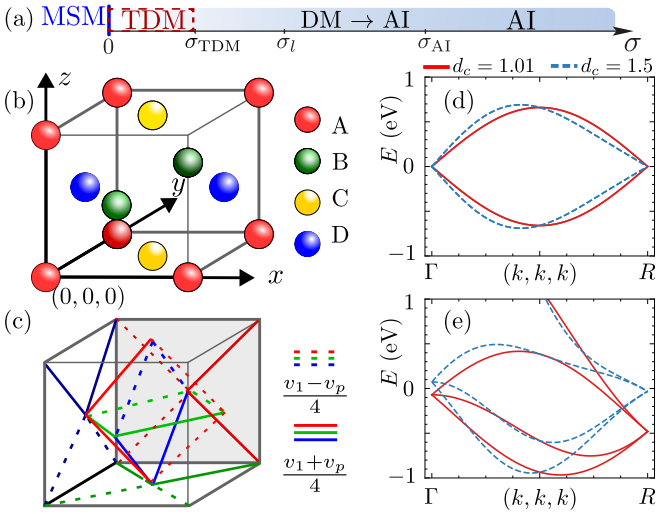

Figure 1. (a) Schematic phase diagram found in this work, including the multifold semimetal (MSM), topological diffusive metal (TDM), the diffusive metal (DM) and the Anderson insulator (AI) phases, as a function of the disorder variance σ. The TDM is signaled by in-gap states of the localizer as well as a finite DOS at E_F, typical of a diffusive metal, until $\sigma_{\rm TDM}$, defined in Fig. 4. σ_l and $\sigma_{\rm AI}$ delimit the crossover between the diffusive metal and the Anderson insulator and are defined in Fig. 3. (b) Orbitals of the crystalline unit cell. (c) Shows the nearest-neighbor inter-orbital hoppings $\frac{v_1 \pm v_p}{4}$ represented by solid and dashed lines. The color denotes hoppings between different set of orbitals: red for A-B/C-D, blue for A-D/B-C and green for A-C/B-D. (d) Band-structure for parameter regime (1) with $v_1 = v_2 = 0, v_p = -0.762$, (e) Band-structure for parameter regime (2), a-RhSi, with $v_1 = 0.55, v_2 = 0.16, v_p = -0.762$. Solid and dashed curves correspond to maximum hopping radii $d_c = 1.01, 1.5$, respectively. In (c), the spectrum is doubly degenerate with two double-Weyl fermions occurring at Γ and R points. In (d), a-RhSi regime, we see a threefold fermion at Γ point and a double-Weyl fermion at R point.

$\tilde{v}_p(d) = v_p/d$. In contrast, the hopping $\tilde{v}_p(\theta,\phi)$ depends on the type of orbitals that form the bond as detailed in the SM [75]. The $\tilde{v}_\alpha$ recover the original tight-binding Hamiltonian in the crystalline limit when $\sigma \to 0$ [55, 75].

The step function Θ in (2) ensures that the maximum distance between two sites is d_c, whose effect is shown in Figs. 1c,d. Notably for a-RhSi longer range hoppings reduce the energy difference between threefold and double Weyl fermions. In our simulations, $d_c = 1.5$ which allows to account for longer-range hoppings (see SM [75]).

Lastly, to account for possible potential disorder [48], we add random onsite potentials drawn from the Gaussian distribution Eq. (1). Thus, our model accounts for all types of disorder expected in amorphous solids: on-site, hopping and structural disorder.

Spectral properties – The density of states (DOS) characterizes disordered topological semimetals [15], and can

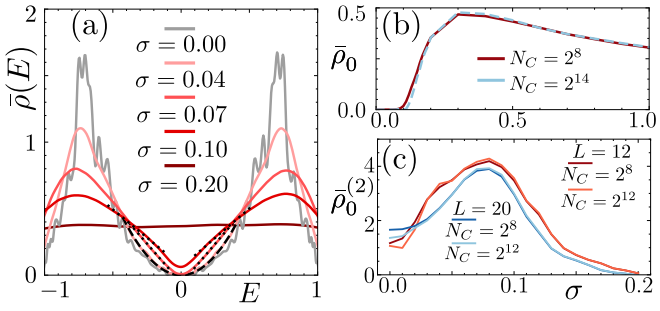

Figure 2. (a) $\rho(E)$ vs E as a function of σ. Dashed and dotted lines represent fit functions αE^2 and $\alpha + \beta|E|$, respectively. (b) The averaged zero-energy DOS $\bar{\rho}_0$ as a function of disorder strength σ; ρ_0 becomes nonzero at $\sigma \approx 0.1$. (c) $\bar{\rho}^{(2)}(0)$ vs σ peaks around $\sigma_c = 0.08$ independent of system size ($L = 12, 20$) and KPM order N_C. We define $\bar{\rho}^{(2)}(0) = \sum_{\lambda=1}^{N_{\rm dis}} (\rho^\lambda)^{(2)}(0)$ where $(\rho^\lambda)^{(2)}(0)$ is estimated from a fit $\rho^\lambda(E) = \rho_0^\lambda + (\rho^\lambda)^{(2)}(0)E^2$ in the energy range $(-0.2, 0.2)$ for independent disorder realizations λ.

be defined as

$$\rho^\lambda(E) = \frac{1}{V}\sum_n \delta(E - E_n), \tag{3}$$

where λ labels a disorder realization, n runs over all states of the system, and $V = 4L^3$ for a cubic system with L unit cells in each direction. For every disorder realization, the DOS is calculated using the numerically efficient kernel polynomial method (KPM), which relies on a Chebyshev polynomial expansion up to order N_C [76]. In the following, we study the disorder averaged DOS $\bar{\rho}(E) = \frac{1}{\rm N_{dis}} \sum_{\lambda=1}^{\rm N_{dis}} \rho^\lambda(E)$ with $\rm N_{dis} = 16$.

We focus first on regime (1) that has two double Weyl fermions at $E = 0$ in the crystalline limit. Figs. 2a and b show $\bar{\rho}(E)$ for different disorder strengths and $\bar{\rho}_0 \equiv \bar{\rho}(E = 0)$ for different KPM orders N_C, respectively. We see that for $\sigma \lessapprox 0.04$, $\bar{\rho}(E) \to |E|^2$, as in periodic systems with (double-) Weyl fermions at the same energy. Once the disorder strength is increased up to $\sigma \approx 0.07$, $\bar{\rho} \propto |E|$ close to $E = 0$. Additionally, at $\sigma = 0.1$ the DOS at $E = 0$ becomes nonzero. Fig. 2b reveals that $\bar{\rho}_0 \neq 0$ for $\sigma \geq 0.1$ signaling that the system becomes a diffusive metal, a phase with constant DOS in a range of energies.

This behavior suggests a putative quantum critical point (QCP) at a certain σ_c, where the semimetal phase is replaced by a diffusive metal [13, 16]. To study this phase transition in more detail, Fig. 2c shows $\bar{\rho}_0^{(2)}$, extracted from a low energy fit $\bar{\rho}(E) = \bar{\rho}_0 + \bar{\rho}_0^{(2)} E^2$ to the DOS [13]. It remains finite with a maximum at $\sigma_c \approx 0.08$, that shifts little with increasing system size or the order of the KPM expansion. This non-divergent behavior signals that the putative QCP is avoided [13].

Avoiding such QCP is enabled by the presence of statistically-rare states [13]. Rare states are low-energy eigenstates that are quasi-bounded to the real space regions with uncharacteristically large potential strengths that are statistically rare. In the thermodynamic limit, these statistically rare events are likely to occur for any nonzero σ. As a result, $\bar{\rho}_0$ becomes exponentially small in disorder strength but nonzero, implying a crossover from semimetal to diffusive metal phase instead of a perturbative transition [13, 16], see SM [75] for more details.

Importantly, it is the vanishing DOS at the band crossing that makes rare-states dominate the physics of disordered Weyl semimetals. The DOS vanishes at $E = 0$ for parameter regime (1), where two Weyl nodes coexist at the Fermi level, but not for the a-RhSi regime (2). In the latter, disorder can couple states without energy penalty [77], turning the a-RhSi regime into a diffusive metal for any infinitesimal amount of disorder.

Anderson localization – While eigenstates of diffusive metals are extended, sufficiently strong disorder will turn metallic systems into Anderson insulators with localized eigenstates [15]. Localized states interact weakly, thus producing an uncorrelated energy spectrum that obeys a Poisson distribution function [78]. On the metallic side, the overlap of delocalized states leads to the repulsion of associated energy levels. For spinless and time-reversal symmetric systems, like a-RhSi, such a spectrum falls under the Gaussian Orthogonal Ensemble (GOE) of random matrices [79].

To distinguish between metallic and insulating regimes, we calculate the adjacent energy level spacing ratio and the inverse participation ratio (IPR) of states at the Fermi level E_F. The adjacent level spacing ratio is defined as

$$r = \frac{1}{N_E - 2}\sum_n \frac{\min(E_{n,n-1}, E_{n+1,n})}{\max(E_{n,n-1}, E_{n+1,n})}, \tag{4}$$

where $E_{n,m} = E_n - E_m$ and the energy levels are arranged such that $E_n > E_{n-1}$. The sum is performed over N_E energy levels within the interval $[E_F - \Delta E, E_F + \Delta E]$. The GOE and Poisson spectra have $r_{\rm GOE} \approx 0.54$ and $r_{\rm P} \approx 0.39$, respectively [80]. To quantify the localization of a set of eigenstates near E_F, we use the IPR, defined as $\text{IPR} = \frac{1}{N_E}\sum_n \sum_{\mathbf{r}} |\Psi_n(\mathbf{r})|^4$. Here Ψ_n is the eigenstate corresponding to n-th eigenvalue, and the sum is taken over the same energy window N_E as for r. The IPR is close to zero for delocalized states and unity for localized states.

In the following, we focus on small system sizes $L = 6, 8$ where exact diagonalization is possible. We choose first to quantify the localization of double-Weyl fermions in parameter regime (1). We fix $E_F = 0, \Delta E = 0.1$ and calculate the disorder averaged r, $\bar{r} = \frac{1}{\rm N_{dis}} \sum_{\lambda=1}^{\rm N_{dis}} r^\lambda$. Here, $\rm N_{dis} = 101$ for $L = 6$ and $\rm N_{dis} = 51$ for $L = 8$. The results are shown in Fig. 3a, where we see that $\bar{r} \approx 0.54$, as expected for the GOE, in the range $0 < \sigma < \sigma_l$ where $\sigma_l \approx 1.2$. For $\sigma > \sigma_{\rm AI} \approx 3.95$, $\bar{r}$ transitions to ≈ 0.39 expected for the Poisson class. This transition is also

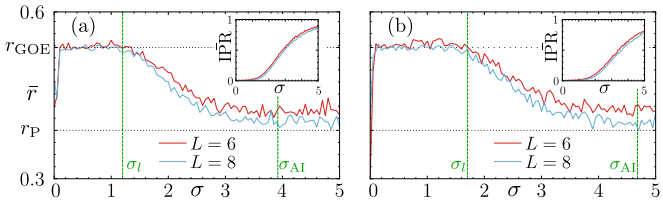

Figure 3. Panels (a) and (b) show adjacent level spacing ratios at $E_F = 0$ as a function of disorder strength σ for a system in parameter regime (1) and a-RhSi regime, respectively. Here, $r_{\rm GOE} = 0.536$ and $r_{\rm P} = 0.387$ are represented by dotted gray lines, while dashed green lines represent disorder strengths σ_l and $\sigma_{\rm AI}$. The insets show the inverse participation ratios at the Fermi energy of respective panels.

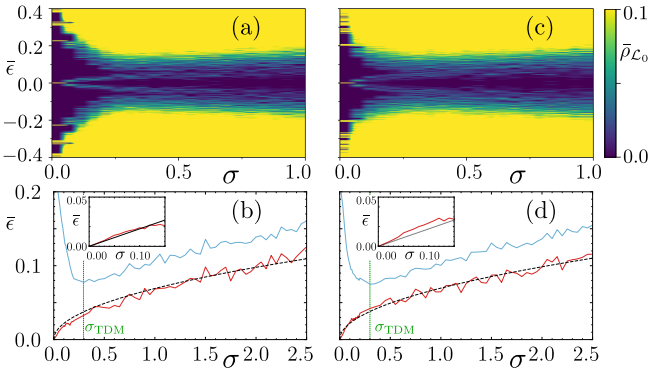

Figure 4. (a) and (c) show the disorder averaged DOS of the operator $\mathcal{L}_0$ as a function of disorder strength σ for regime (1) a-RhSi regime, respectively. Panels (b) and (d) show the disorder averaged energies of the midgap and first-excited states $\bar{\epsilon}_0, \bar{\epsilon}_1$ as a function of σ for the two parameter regimes. Here, dashed green lines represent the topological phase transition point $\sigma_{\rm TDM}$. The dashed black line represents a fit $\bar{\epsilon}_0 = a\sqrt{\sigma}$, where $a = 0.0692$ in regime (1) and $a = 0.0696$ for regime (2). The insets of (b) and (d) show how well $\bar{\epsilon}_0$ matches with the predicted form $\kappa^{0.75}\sigma$ [68] (gray line) in case of small disorder strengths. For all plots $\kappa = 0.1$ and $\mathrm{N_{dis}} = 25$.

reflected in the change of the disorder averaged IPR, $\bar{\rm IPR}$, shown in the inset of Fig. 3a. We see that $\bar{\rm IPR}$ remains close to zero up until σ_l, after which it starts increasing with disorder. Stronger disorder strengths ($\sigma > \sigma_{\rm AI}$) localize further the states at E_F, where $\bar{\rm IPR} \to 1$.

To study the a-RhSi regime, we choose $E_F = 0$ and $\Delta E = 0.1$ in order to probe localization at energies comparable to the threefold fermion. We show the disorder averaged $\bar{r}$ and $\bar{\rm IPR}$ in Fig. 3b and its inset, respectively. Because of the enhanced DOS compared to regime (1), diffusive metal phase persists up to a larger disorder strength $\sigma_l \approx 1.7$. The Anderson localization is also delayed to stronger disorder strengths $\sigma_{\rm AI} \approx 4.6$.

Topological phase diagram – Lastly, we are interested in quantifying to what extent the topological properties of multifold fermions survive disorder. In time-reversal symmetric systems like RhSi, we cannot use real space invariants like the local Chern marker [54] or the Bott index [53], used for time-reversal breaking Weyl semimetals [21, 81]. Instead, we resort to the recently introduced spectral localizer [67–69].

In three-dimensions, the spectral localizer is defined as [67, 69]

$$\mathcal{L}(\mathbf{r}, E) = \kappa \sum_{j=1}^{d} \gamma_j (X_j - x_j \mathbb{I}) + \gamma_{d+1}(H - E\mathbb{I}), \qquad (5)$$

where X_j are position operators corresponding to the Hamiltonian H, and the matrices γ_j form a Clifford representation $\{\gamma_j, \gamma_i\} = 2\delta_{ij}$. We choose $\gamma_j = \tau_z \sigma_j$ for $j = 1, 2, 3$ and $\gamma_4 = \tau_x \sigma_0$, where σ and τ are Pauli matrices. The coefficient κ fixes the units and relative weights between X_j and H [65, 69]. While the spectral localizer can be evaluated at any position $\mathbf{r}_j$ and energy E, here we choose $\mathbf{r}_j$ to be at the center of our system ($\mathbf{r}_j = \mathbf{0}$) in order to probe their bulk properties, and $E = 0$. In the following, we abbreviate $\mathcal{L}(\mathbf{0}, 0)$ with $\mathcal{L}_0$.

The spectrum of $\mathcal{L}_0$ consists of pairs $(\epsilon, -\epsilon)$ because $\mathcal{L}_0$ obeys chiral symmetry $\mathcal{C} = \tau_y \sigma_0 \mathbb{I}$. In the crystalline limit, the parameter regime (1) yields four states pinned at $\epsilon = 0$, that are separated from the remaining states by a gap of order $\sqrt{\kappa}$. Using a semi-classical analysis of the operator $\mathcal{L}^2$ [68, 75], it is possible to show analytically that each Weyl node contributes exactly one zero mode [68]. We have generalized such an analysis [75] for the case of a system with threefold and double-Weyl fermions, i.e., the a-RhSi regime, predicting four midgap modes as well [75]. The number of midgap modes of $\mathcal{L}_0$ can be thus used to signal multifold fermions in both regimes, as trivial metals present different midgap mode counting [82].

To study how $\mathcal{L}_0$ changes with disorder, we focus on its DOS $\rho_{\mathcal{L}_0}$, calculated using the KPM [76] with an energy resolution $\Delta\epsilon = 5 \times 10^{-4}$ ($N_C \sim 6000$). The system size is $L = 12$ (we obtain similar results for $L = 20$) and we consider $\mathrm{N_{dis}} = 25$ disorder realizations. Fig. 4a shows the disorder-averaged DOS $\bar{\rho}_{\mathcal{L}_0}$, as a function of disorder strength σ for regime (1). From Fig. 4a, we see that as σ is increased, the four zero-energy states split into a pair of peaks that move away from $\epsilon = 0$ in a symmetric fashion. In parallel, disorder reduces the spectral localizer gap and, at around $\sigma_{\rm TDM} = 0.3$, the energies of the midgap and first-excited states become comparable, indicating the transition into a trivial diffusive metal. The existence of the topological in-gap modes of $\mathcal{L}_0$ for $\sigma < \sigma_{\rm TDM}$ defines the topological diffusive metal phase (see Fig. 1a).

The transition from a topological to a trivial diffusive metal is also apparent by tracking, for every disorder realization λ, the peak positions $\epsilon_0^\lambda, \epsilon_1^\lambda$ corresponding to the midgap mode and the first excited state, respectively. In Fig. 4b, we plot their disorder averaged energy $\bar{\epsilon}_{0,1} = \frac{1}{\mathrm{N_{dis}}} \sum_{\lambda=1}^{\mathrm{N_{dis}}} \epsilon_{0,1}^\lambda$ as a function of σ. We see

that $\bar{\epsilon}_0$ and $\bar{\epsilon}_1$ approach each other for $\sigma < \sigma_{\mathrm{TDM}}$ and evolve together, without crossing, for $\sigma \gtrapprox \sigma_{\mathrm{TDM}}$. For small disorder strengths, see inset of Fig. 4b, we find that $\bar{\epsilon}_0 = \sigma\kappa^{3/4}$ consistent with the analytical prediction concerning weakly disordered Weyl semimetals [68]. Moreover, we find that $\bar{\epsilon}_0$ can be fitted with a function $a\sqrt{\sigma}$ ($a \approx 0.07$) in the entire disorder range.

In Figs. 4c,d we show results for the a-RhSi regime. Even though the system supports a threefold fermion in the crystalline limit, $\bar{\rho}_{\mathcal{L}_0}$ behaves similarly to regime (1) with two double-Weyl fermions. In both Fig. 4c and d the gap between midgap and excited modes seems to close for $\sigma_{\mathrm{TDM}} \approx 0.3$. Furthermore, we recover $\bar{\epsilon}_0 = \sigma\kappa^{3/4}$ behavior in the limit of small disorder, as well as $\bar{\epsilon}_0 \propto \sqrt{\sigma}$ for the entire disorder range.

We find that both regimes behave similarly as long the hopping amplitude v_p is the largest energy scale. This condition ensures a sizable difference between the amplitudes of direction dependent nearest-neighbor hoppings $(v_1 \pm v_p)/4$. This condition is met by the RhSi parameters but not for those of a-CoSi, where the parameter v_1 is more than three times larger than the parameter v_p. As a result, the topological properties of a-CoSi are expected to be less robust compared to a-RhSi (see SM [75]).

Conclusion – We have shown that a topological type of diffusive metal can exist in transition metal monosilicides in the presence of structural, potential and hopping disorder. Characterizing this novel phase required us to extended the recently discovered spectral localizer $\mathcal{L}$ to accommodate multifold fermions. The spectral localizer can be used to signal topological diffusive metals in any symmetry class, including those for which other real-space methods yield trivial results or are ill-defined.

Our analysis highlights a-RhSi as a more robust platform than a-CoSi to realize the topological diffusive metal due to a larger anisotropy between nearest neighbor hoppings. Looking forward, it is worth studying whether such stability permeates to physical properties such as the photogalvanic effect or negative magneto-resistance.

Acknowledgments – We thank Q. Marsal, H. Schulz-Baldes, J. Wilson and D. Carpentier for discussions. A.G.G. and S. F. acknowledge financial support from the European Union Horizon 2020 research and innovation program under grant agreement No. 829044 (SCHINES). A. G. G. is also supported by the European Research Council (ERC) Consolidator grant under grant agreement No. 101042707 (TOPOMORPH). The Kwant code [83] used to generate our results is available at [84].

* selma.franca@neel.cnrs.fr
† adolfo.grushin@neel.cnrs.fr

[1] N. P. Armitage, E. J. Mele, and A. Vishwanath, Weyl and Dirac semimetals in three-dimensional solids, Rev. Mod. Phys. **90**, 015001 (2018).
[2] E. Fradkin, Critical behavior of disordered degenerate semiconductors. I. models, symmetries, and formalism, Phys. Rev. B **33**, 3257 (1986).
[3] E. Fradkin, Critical behavior of disordered degenerate semiconductors. II. spectrum and transport properties in mean-field theory, Phys. Rev. B **33**, 3263 (1986).
[4] A. Altland and D. Bagrets, Effective field theory of the disordered Weyl semimetal, Phys. Rev. Lett. **114**, 257201 (2015).
[5] S. V. Syzranov, P. M. Ostrovsky, V. Gurarie, and L. Radzihovsky, Critical exponents at the unconventional disorder-driven transition in a Weyl semimetal, Phys. Rev. B **93**, 155113 (2016).
[6] J. H. Pixley, P. Goswami, and S. Das Sarma, Disorder-driven itinerant quantum criticality of three-dimensional massless Dirac fermions, Phys. Rev. B **93**, 085103 (2016).
[7] A. Altland and D. Bagrets, Theory of the strongly disordered Weyl semimetal, Phys. Rev. B **93**, 075113 (2016).
[8] B. Sbierski, K. S. C. Decker, and P. W. Brouwer, Weyl node with random vector potential, Phys. Rev. B **94**, 220202 (2016).
[9] T. Louvet, D. Carpentier, and A. A. Fedorenko, On the disorder-driven quantum transition in three-dimensional relativistic metals, Phys. Rev. B **94**, 220201 (2016).
[10] T. Louvet, D. Carpentier, and A. A. Fedorenko, New quantum transition in Weyl semimetals with correlated disorder, Phys. Rev. B **95**, 014204 (2017).
[11] X. Luo, B. Xu, T. Ohtsuki, and R. Shindou, Quantum multicriticality in disordered Weyl semimetals, Phys. Rev. B **97**, 045129 (2018).
[12] I. Balog, D. Carpentier, and A. A. Fedorenko, Disorder-driven quantum transition in relativistic semimetals: Functional renormalization via the porous medium equation, Phys. Rev. Lett. **121**, 166402 (2018).
[13] J. Pixley and J. H. Wilson, Rare regions and avoided quantum criticality in disordered Weyl semimetals and superconductors, Annals of Physics **435**, 168455 (2021).
[14] R. Nandkishore, D. A. Huse, and S. L. Sondhi, Rare region effects dominate weakly disordered three-dimensional Dirac points, Phys. Rev. B **89**, 245110 (2014).
[15] J. H. Pixley, P. Goswami, and S. Das Sarma, Anderson localization and the quantum phase diagram of three dimensional disordered Dirac semimetals, Phys. Rev. Lett. **115**, 076601 (2015).
[16] J. H. Pixley, D. A. Huse, and S. Das Sarma, Rare-region-induced avoided quantum criticality in disordered three-dimensional Dirac and Weyl semimetals, Phys. Rev. X **6**, 021042 (2016).
[17] V. Gurarie, Theory of avoided criticality in quantum motion in a random potential in high dimensions, Phys. Rev. B **96**, 014205 (2017).
[18] M. Buchhold, S. Diehl, and A. Altland, Vanishing density of states in weakly disordered Weyl semimetals, Phys. Rev. Lett. **121**, 215301 (2018).
[19] M. Buchhold, S. Diehl, and A. Altland, Nodal points of Weyl semimetals survive the presence of moderate disorder, Phys. Rev. B **98**, 205134 (2018).
[20] J. H. Wilson, D. A. Huse, S. Das Sarma, and J. H. Pixley, Avoided quantum criticality in exact numerical simulations of a single disordered Weyl cone, Phys. Rev. B **102**, 100201 (2020).
[21] Y.-B. Yang, T. Qin, D.-L. Deng, L.-M. Duan, and Y. Xu, Topological amorphous metals, Phys. Rev. Lett. **123**,

076401 (2019).
[22] J. L. Mañes, Existence of bulk chiral fermions and crystal symmetry, Phys. Rev. B **85**, 155118 (2012).
[23] B. Bradlyn, J. Cano, Z. Wang, M. G. Vergniory, C. Felser, R. J. Cava, and B. A. Bernevig, Beyond Dirac and Weyl fermions: Unconventional quasiparticles in conventional crystals, Science **353**, aaf5037 (2016).
[24] P. Tang, Q. Zhou, and S.-C. Zhang, Multiple types of topological fermions in transition metal silicides, Phys. Rev. Lett. **119**, 206402 (2017).
[25] G. Chang, B. J. Wieder, F. Schindler, D. S. Sanchez, I. Belopolski, S.-M. Huang, B. Singh, D. Wu, T.-R. Chang, T. Neupert, S.-Y. Xu, H. Lin, and M. Z. Hasan, Topological quantum properties of chiral crystals, Nature Materials **17**, 978 (2018).
[26] D. S. Sanchez, I. Belopolski, T. A. Cochran, X. Xu, J.-X. Yin, G. Chang, W. Xie, K. Manna, V. Süß, C.-Y. Huang, N. Alidoust, D. Multer, S. S. Zhang, N. Shumiya, X. Wang, G.-Q. Wang, T.-R. Chang, C. Felser, S.-Y. Xu, S. Jia, H. Lin, and M. Z. Hasan, Topological chiral crystals with helicoid-arc quantum states, Nature **567**, 500 (2019).
[27] D. Takane, Z. Wang, S. Souma, K. Nakayama, T. Nakamura, H. Oinuma, Y. Nakata, H. Iwasawa, C. Cacho, T. Kim, K. Horiba, H. Kumigashira, T. Takahashi, Y. Ando, and T. Sato, Observation of chiral fermions with a large topological charge and associated Fermi-arc surface states in CoSi, Phys. Rev. Lett. **122**, 076402 (2019).
[28] Z. Rao, H. Li, T. Zhang, S. Tian, C. Li, B. Fu, C. Tang, L. Wang, Z. Li, W. Fan, J. Li, Y. Huang, Z. Liu, Y. Long, C. Fang, H. Weng, Y. Shi, H. Lei, Y. Sun, T. Qian, and H. Ding, Observation of unconventional chiral fermions with long Fermi arcs in CoSi, Nature **567**, 496 (2019).
[29] N. B. M. Schröter, D. Pei, M. G. Vergniory, Y. Sun, K. Manna, F. de Juan, J. A. Krieger, V. Süss, M. Schmidt, P. Dudin, B. Bradlyn, T. K. Kim, T. Schmitt, C. Cacho, C. Felser, V. N. Strocov, and Y. Chen, Chiral topological semimetal with multifold band crossings and long Fermi arcs, Nature Physics **15**, 759 (2019).
[30] D. S. Wu, Z. Y. Mi, Y. J. Li, W. Wu, P. L. Li, Y. T. Song, G. T. Liu, G. Li, and J. L. Luo, Single crystal growth and magnetoresistivity of topological semimetal CoSi*, Chinese Phys. Lett. **36**, 077102 (2019).
[31] Z. Ni, K. Wang, Y. Zhang, O. Pozo, B. Xu, X. Han, K. Manna, J. Paglione, C. Felser, A. G. Grushin, F. de Juan, E. J. Mele, and L. Wu, Giant topological longitudinal circular photo-galvanic effect in the chiral multifold semimetal CoSi, Nature Communications **12**, 154 (2021).
[32] H.-C. Hsu, I. C. Fulga, and J.-S. You, Disorder effects on triple-point fermions, Phys. Rev. B **106**, 245118 (2022).
[33] R. Kikuchi and A. Yamakage, Electrical conductivity and screening effect of spin-1 chiral fermions scattered by charged impurities, Preprint at https://arxiv.org/abs/2305.11631 (2023).
[34] A. Agarwala and V. B. Shenoy, Topological insulators in amorphous systems, Phys. Rev. Lett. **118**, 236402 (2017).
[35] S. Mansha and Y. D. Chong, Robust edge states in amorphous gyromagnetic photonic lattices, Phys. Rev. B **96**, 121405 (2017).
[36] N. P. Mitchell, L. M. Nash, D. Hexner, A. M. Turner, and W. T. M. Irvine, Amorphous topological insulators constructed from random point sets, Nature Physics **14**, 380 (2018).
[37] G.-W. Chern, Topological insulator in an atomic liquid, Europhysics Letters **126**, 37002 (2019).
[38] Q. Marsal, D. Varjas, and A. G. Grushin, Topological Weaire–Thorpe models of amorphous matter, Proceedings of the National Academy of Sciences **117**, 30260 (2020).
[39] I. Sahlberg, A. Weststrom, K. Pöyhönen, and T. Ojanen, Topological phase transitions in glassy quantum matter, Phys. Rev. Res. **2**, 013053 (2020).
[40] M. N. Ivaki, I. Sahlberg, and T. Ojanen, Criticality in amorphous topological matter: Beyond the universal scaling paradigm, Phys. Rev. Res. **2**, 043301 (2020).
[41] M. Costa, G. R. Schleder, M. Buongiorno Nardelli, C. Lewenkopf, and A. Fazzio, Toward realistic amorphous topological insulators, Nano Letters **19**, 8941 (2019).
[42] B. Focassio, G. R. Schleder, M. Costa, A. Fazzio, and C. Lewenkopf, Structural and electronic properties of realistic two-dimensional amorphous topological insulators, 2D Materials **8**, 025032 (2021).
[43] C. Wang, T. Cheng, Z. Liu, F. Liu, and H. Huang, Structural amorphization-induced topological order, Phys. Rev. Lett. **128**, 056401 (2022).
[44] J. Ma and H. Huang, Amorphous Kane-Mele model in disordered hyperuniform two-dimensional networks, Phys. Rev. B **106**, 195150 (2022).
[45] T. Mano and T. Ohtsuki, Application of convolutional neural network to quantum percolation in topological insulators, J. Phys. Soc. Jpn. **88**, 123704 (2019).
[46] P. Mukati, A. Agarwala, and S. Bhattacharjee, Topological and conventional phases of a three-dimensional electronic glass, Phys. Rev. B **101**, 035142 (2020).
[47] P. Corbae, S. Ciocys, D. Varjas, E. Kennedy, S. Zeltmann, M. Molina-Ruiz, S. M. Griffin, C. Jozwiak, Z. Chen, L.-W. Wang, A. M. Minor, M. Scott, A. G. Grushin, A. Lanzara, and F. Hellman, Observation of spin-momentum locked surface states in amorphous Bi_2Se_3, Nature Materials **22**, 200 (2023).
[48] H. Spring, A. R. Akhmerov, and D. Varjas, Amorphous topological phases protected by continuous rotation symmetry, SciPost Phys. **11**, 022 (2021).
[49] A. Agarwala, V. Juričić, and B. Roy, Higher-order topological insulators in amorphous solids, Phys. Rev. Res. **2**, 012067 (2020).
[50] J.-H. Wang, Y.-B. Yang, N. Dai, and Y. Xu, Structural-disorder-induced second-order topological insulators in three dimensions, Phys. Rev. Lett. **126**, 206404 (2021).
[51] T. Peng, C.-B. Hua, R. Chen, Z.-R. Liu, H.-M. Huang, and B. Zhou, Density-driven higher-order topological phase transitions in amorphous solids, Phys. Rev. B **106**, 125310 (2022).
[52] Y.-L. Tao, J.-H. Wang, and Y. Xu, Average symmetry protected higher-order topological amorphous insulators, Preprint at https://arxiv.org/abs/2306.02246 (2023).
[53] T. A. Loring and M. B. Hastings, Disordered topological insulators via C*-algebras, Europhysics Letters **92**, 67004 (2011).
[54] R. Bianco and R. Resta, Mapping topological order in coordinate space, Phys. Rev. B **84**, 241106 (2011).
[55] G. Chang, S.-Y. Xu, B. J. Wieder, D. S. Sanchez, S.-M. Huang, I. Belopolski, T.-R. Chang, S. Zhang, A. Bansil, H. Lin, and M. Z. Hasan, Unconventional chiral fermions and large topological Fermi arcs in RhSi, Phys. Rev. Lett.

119, 206401 (2017).
[56] D. A. Pshenay-Severin, Y. V. Ivanov, A. A. Burkov, and A. T. Burkov, Band structure and unconventional electronic topology of CoSi, J. Phys.: Condens. Matter **30**, 135501 (2018).
[57] F. de Juan, A. Grushin, T. Morimoto, and J. Moore, Quantized circular photogalvanic effect in Weyl semimetals, Nat. Commun. **8**, 15995 (2017).
[58] F. Flicker, F. de Juan, B. Bradlyn, T. Morimoto, M. G. Vergniory, and A. G. Grushin, Chiral optical response of multifold fermions, Phys. Rev. B **98**, 155145 (2018).
[59] D. Rees, K. Manna, B. Lu, T. Morimoto, H. Borrmann, C. Felser, J. E. Moore, D. H. Torchinsky, and J. Orenstein, Helicity-dependent photocurrents in the chiral Weyl semimetal RhSi, Science Advances **6**, eaba0509 (2020).
[60] Z. Ni, B. Xu, M.-Á. Sánchez-Martínez, Y. Zhang, K. Manna, C. Bernhard, J. W. F. Venderbos, F. de Juan, C. Felser, A. G. Grushin, and L. Wu, Linear and nonlinear optical responses in the chiral multifold semimetal RhSi, npj Quantum Materials **5**, 96 (2020).
[61] C. Guo, L. Hu, C. Putzke, J. Diaz, X. Huang, K. Manna, F.-R. Fan, C. Shekhar, Y. Sun, C. Felser, C. Liu, B. A. Bernevig, and P. J. W. Moll, Quasi-symmetry-protected topology in a semi-metal, Nature Physics **18**, 813 (2022).
[62] L.-H. Hu, C. Guo, Y. Sun, C. Felser, L. Elcoro, P. J. W. Moll, C.-X. Liu, and B. A. Bernevig, Hierarchy of quasisymmetries and degeneracies in the CoSi family of chiral crystal materials, Phys. Rev. B **107**, 125145 (2023).
[63] A. Molinari, F. Balduini, L. Rocchino, R. Wawrzyńczak, M. Sousa, H. Bui, C. Lavoie, V. Stanic, J. Jordan-Sweet, M. Hopstaken, S. Tchoumakov, S. Franca, J. Gooth, S. Fratini, A. G. Grushin, C. Zota, B. Gotsmann, and H. Schmid, Disorder-induced magnetotransport anomalies in amorphous and textured $Co_{1-x}Si_x$ semimetal thin films, ACS Appl. Electron. Mater. **5**, 2624 (2023).
[64] T. A. Loring, K-theory and pseudospectra for topological insulators, Annals of Physics **356**, 383 (2015).
[65] T. A. Loring, A guide to the Bott index and localizer index, Preprint at https://arxiv.org/abs/1907.11791 (2019).
[66] T. Loring and H. Schulz-Baldes, The spectral localizer for even index pairings, J. Noncommut. Geom. **14**, 1–23 (2020), arXiv:1802.04517.
[67] H. Schulz-Baldes and T. Stoiber, Invariants of disordered semimetals via the spectral localizer, Europhysics Letters **136**, 27001 (2022).
[68] H. Schulz-Baldes and T. Stoiber, Spectral localization for semimetals and Callias operators, Preprint at https://arxiv.org/abs/2203.15014 (2022).
[69] A. Cerjan and T. A. Loring, Local invariants identify topology in metals and gapless systems, Phys. Rev. B **106**, 064109 (2022).
[70] R. Zallen, *The Physics of Amorphous Solids* (Wiley-VCH, 1998).
[71] C.-T. Toh, H. Zhang, J. Lin, A. S. Mayorov, Y.-P. Wang, C. M. Orofeo, D. B. Ferry, H. Andersen, N. Kakenov, Z. Guo, I. H. Abidi, H. Sims, K. Suenaga, S. T. Pantelides, and B. Özyilmaz, Synthesis and properties of free-standing monolayer amorphous carbon, Nature **577**, 199 (2020).
[72] P. Corbae, J. D. Hannukainen, Q. Marsal, D. Muñoz-Segovia, and A. G. Grushin, Amorphous topological matter: theory and experiment, Preprint at https://arxiv.org/abs/2301.04176 (2023).
[73] S. T. Ciocys, Q. Marsal, P. Corbae, D. Varjas, E. Kennedy, M. Scott, F. Hellman, A. G. Grushin, and A. Lanzara, Establishing coherent momentum-space electronic states in locally ordered materials, Preprint at https://arxiv.org/abs/2302.05945 (2023).
[74] B. Xu, Z. Fang, M. Ángel Sánchez-Martínez, J. W. F. Venderbos, Z. Ni, T. Qiu, K. Manna, K. Wang, J. Paglione, C. Bernhard, C. Felser, E. J. Mele, A. G. Grushin, A. M. Rappe, and L. Wu, Optical signatures of multifold fermions in the chiral topological semimetal CoSi, Proceedings of the National Academy of Sciences **117**, 27104 (2020).
[75] In the Supplemental Material, we provide Bloch Hamiltonians of RhSi/CoSi and discuss how longer range hoppings alter the band-structure. We then show proofs of the existence of rare states in amorphous RhSi, before discussing in detail the spectral properties of the spectral localizer calculated for systems with double Weyl fermions and threefold fermions. Finally, we discuss how our conclusions discussed in the main text differ in case of a-CoSi.
[76] A. Weiße, G. Wellein, A. Alvermann, and H. Fehske, The kernel polynomial method, Rev. Mod. Phys. **78**, 275 (2006).
[77] M. Trescher, B. Sbierski, P. W. Brouwer, and E. J. Bergholtz, Tilted disordered Weyl semimetals, Phys. Rev. B **95**, 045139 (2017).
[78] E. Akkermans and G. Montamboux, *Mesoscopic Physics of Electrons and Photons* (Cambridge University Press, 2007).
[79] C. W. J. Beenakker, Random-matrix theory of quantum transport, Rev. Mod. Phys. **69**, 731 (1997).
[80] Y. Y. Atas, E. Bogomolny, O. Giraud, and G. Roux, Distribution of the ratio of consecutive level spacings in random matrix ensembles, Phys. Rev. Lett. **110**, 084101 (2013).
[81] Z.-Q. Zhang, B.-L. Wu, C.-Z. Chen, and H. Jiang, Global phase diagram of disordered higher-order Weyl semimetals, Phys. Rev. B **104**, 014203 (2021).
[82] S. Franca and A. G. Grushin, Obstructions in trivial metals as topological insulator zero-modes, Preprint at https://arxiv.org/abs/2304.01983 (2023).
[83] C. W. Groth, M. Wimmer, A. R. Akhmerov, and X. Waintal, Kwant: a software package for quantum transport, New J. Phys. **16**, 063065 (2014).
[84] S. Franca and A. G. Grushin, Topological diffusive metal in amorphous transition metal mono-silicides, Zenodo 10.5281/zenodo.8095821 (2023).

Supplemental Material to: Topological diffusive metal in amorphous transition metal mono-silicides

Selma Franca[1,*] and Adolfo G. Grushin[1,†]

[1] *Université Grenoble Alpes, CNRS, Grenoble INP, Institut Néel, 38000 Grenoble, France*

CONTENTS

Appendix A: The Bloch Hamiltonian

We begin this section with classifying, by separation distance, all neighboring orbitals of a crystalline system within radius $d_c = 1.5$, where a is the lattice constant. For each of these distances, we provide a Bloch Hamiltonian for a hopping term between two orbitals. To show that these Bloch Hamiltonians correctly describe the bulk of a finite crystal, we compare their band-structure with the momentum resolved spectral function $A(\mathbf{k}, E)$.

The radial distribution function $g(d)$ gives us the probability of finding two sites separated by distance d. It is defined as

$$g(d) = \frac{\delta n_d}{\delta V_d \eta}, \tag{A1}$$

where δn_d represents the number of sites within a spherical shell of thickness δd and volume $\delta V_d = 4\pi d^2 \delta d$, and η is the bulk density of sites. We measure all distances in units of lattice constant a.

In Fig. S1a, we show $g(d)$ for a crystalline transition metal mono-silicide. We see that the first nearest neighboring orbitals are located at a distance $d = 1/\sqrt{2}$. As discussed in the main text, the hopping between these orbitals are angle dependent as described by the Hamiltonian [1]

$$\begin{aligned}\mathcal{H}_1 =& v_1[\gamma_x\delta_0 \cos\frac{k_x}{2}\cos\frac{k_y}{2} + \gamma_x\delta_x \cos\frac{k_y}{2}\cos\frac{k_z}{2} + \gamma_0\delta_x \cos\frac{k_z}{2}\cos\frac{k_x}{2}]+ \\ & v_p[\gamma_y\delta_z \cos\frac{k_x}{2}\sin\frac{k_y}{2} + \gamma_y\delta_x \cos\frac{k_y}{2}\sin\frac{k_z}{2} + \gamma_0\delta_y \cos\frac{k_z}{2}\sin\frac{k_x}{2}],\end{aligned} \tag{A2}$$

that is written in the basis $\Psi = (c_A, c_B, c_C, c_D)$, where c_α represents the annihilation operator of a particle at orbital $\alpha = A, B, C, D$.

The second nearest-neighbor hopping connects orbitals of the same kind, separated by a distance $d = 1$. These hoppings are captured by the Bloch Hamiltonian [1]

$$\mathcal{H}_2 = v_2[\cos k_x + \cos k_y + \cos k_z]\gamma_0\delta_0. \tag{A3}$$

Since we allow the cut-off radius to vary, our model may involve longer range hoppings. Thus we extend the model of Ref. [1] to incorporate longer-range hoppings, i.e, beyond second-nearest neighbors.

All the longer-range hoppings can also be split into inter-orbital and intra-orbital hoppings, and we determine their amplitudes following Eq. (2) of the main text. For completeness, we repeat it here

$$\tilde{v}_\alpha = \tilde{v}_\alpha(d)\tilde{v}_\alpha(\theta,\phi)\exp\left[1 - \frac{d}{d_\alpha^0}\right]\Theta(d_c - d), \tag{A4}$$

where d, θ and ϕ are the relative spherical coordinates between the positions of the two sites involved in the hopping. Their radial and angular dependencies are given in Table I.

Third nearest-neighbor hoppings connect orbitals at a distance $d = \sqrt{3/2}$. Following Eq. (A4) and Table I, the hopping amplitudes for a crystalline lattice read $\frac{v_1}{\sqrt{3}}\exp[1-\sqrt{3}]$ and $\frac{v_p}{3}\exp[1-\sqrt{3}]$. The corresponding Bloch Hamiltonian reads

* selma.franca@neel.cnrs.fr

† adolfo.grushin@neel.cnrs.fr

α	$\tilde{v}_\alpha(d)$	$\tilde{v}_\alpha(\theta,\phi)$	orbitals involved
1	$v_1/\sqrt{2}d$	1	$A \leftrightarrow B/C/D; B \leftrightarrow C/D, C \leftrightarrow D$
2	v_2/d	1	$A \leftrightarrow A; B \leftrightarrow B; C \leftrightarrow C; D \leftrightarrow D$
p	v_p/d	$\sin\theta\cos\phi$	$A \leftrightarrow B/C \leftrightarrow D$
p	v_p/d	$\sin\theta\sin\phi$	$A \leftrightarrow C/B \leftrightarrow D$
p	v_p/d	$\cos\theta$	$A \leftrightarrow D/B \leftrightarrow C$

Table I. Radial and angular amplitudes of hoppings in transition metal mono-silicides.

$$\mathcal{H}_3 = \frac{v_1}{\sqrt{3}} e^{1-\sqrt{3}} [\gamma_x \delta_0 \cos\frac{k_x}{2}\cos\frac{k_y}{2} 2\cos k_z + \gamma_x \delta_x 2\cos k_x \cos\frac{k_y}{2}\cos\frac{k_z}{2} + \gamma_0 \delta_x \cos\frac{k_z}{2} 2\cos k_y \cos\frac{k_x}{2}] + \frac{v_p}{3} e^{1-\sqrt{3}} [\gamma_y \delta_z \cos\frac{k_x}{2}\sin\frac{k_y}{2} 2\cos k_z + \gamma_y \delta_x 2\cos k_x \cos\frac{k_y}{2}\sin\frac{k_z}{2} + \gamma_0 \delta_y \cos\frac{k_z}{2} 2\cos k_y \sin\frac{k_x}{2}]. \tag{A5}$$

Orbitals of the same type at a distance $d = \sqrt{2}$ are fourth nearest-neighbors, and are related by hopping amplitudes $\frac{v_2}{\sqrt{2}} \exp\left[1-\sqrt{2}\right]$, following Eq. (A4) and Table I. The Bloch Hamiltonian reads

$$\mathcal{H}_4 = 2\frac{v_2}{\sqrt{2}} \exp\left[1-\sqrt{2}\right] [\cos k_x \cos k_y + \cos k_y \cos k_z + \cos k_z \cos k_x] \gamma_0 \delta_0. \tag{A6}$$

In our simulations, we choose a cutoff at $d_c = 1.5$ such that the Bloch Hamiltonian $\mathcal{H} = \mathcal{H}_1 + \mathcal{H}_2 + \mathcal{H}_3 + \mathcal{H}_4$ describes bulk properties of a crystalline transition metal mono-silicide. In the following, we focus on RhSi in parameter regime (2). Its band-structure is shown in Fig. S1b. Compared to Ref. [1], where $\mathcal{H} = \mathcal{H}_1 + \mathcal{H}_2$, we see that when longer-range hoppings are added the threefold fermion at Γ is closer in energy to the double-Weyl fermion at R.

To verify that this band-structure accurately describes the bulk of the constructed crystalline system, we calculate the momentum resolved spectral function $A(\mathbf{k}, E)$ for a finite system. The spectral function is calculated by projecting the real space spectral function onto a plane-wave basis [2]

$$A(\mathbf{k}, E) = -\frac{1}{\pi} \mathrm{Im} \left\langle \mathbf{k} \middle| \frac{1}{\mathrm{H} - \mathrm{E}} \middle| \mathbf{k} \right\rangle, \tag{A7}$$

where $\mathrm{H} = \mathrm{H}_1 + \mathrm{H}_2 + \mathrm{H}_3 + \mathrm{H}_4$ and $\mathrm{H}_1, \mathrm{H}_2, \mathrm{H}_3, \mathrm{H}_4$ are real space tight-binding Hamiltonians deduced from Eqs. (A2), (A3), (A5) and (A6), respectively. Moreover $|\mathbf{k}\rangle = \exp[i\mathbf{k}\mathbf{r}_n]$ at site n with position $\mathbf{r}_n$. The spectral function can be measured in angle-resolved photoemission (ARPES) experiments, where momentum $\mathbf{k}$ represents the momentum of the photo-emitted electron [2].

For a system with 20^3 unit cells and under periodic boundary conditions (PBCs), we plot $A(\mathbf{k}, E)$ in Fig. S1c. We observe that the spectral function calculated with H captures well the energies of threefold and double-Weyl fermions in Fig. S1b, calculated with $\mathcal{H}$, as well as the bandwidth of each band.

Appendix B: Rare states

In this section, we demonstrate the existence of rare states [3] in a-RhSi in parameter regime (1).

In this parameter regime, the density of states of the crystalline system vanishes at $E = 0$. Once disorder strength σ is non-zero, statistically rare regions, with exceptionally strong disorder strength, are possible. Because $\rho(E = 0) = 0$, these regions may trap states at low energies that we call rare states. To confirm the existence of these rare states for our amorphous systems, we follow the procedures outlined in Ref [3].

In finite systems, the energy scales of rare states and the double-Weyl fermions are comparable thus complicating the detection of rare states. For this reason, we study the spectra of infinite systems obtained by imposing twisted boundary conditions. These boundary conditions assume that hoppings between outermost orbitals belonging to different surfaces are $v_\alpha \exp[i\theta]$ ($\alpha = 1, 2, p$), where θ is called the twist angle. For $\theta = 0/\pi$, we say the system in under periodic/anti-periodic boundary conditions. As explained in Ref [3], combining appropriate boundary conditions with different system sizes we can maximally separate the energy scales of double-Weyl fermions and disorder induced rare-states.

In the following, we consider a crystalline system with an even number of unit cells L in all directions. In the

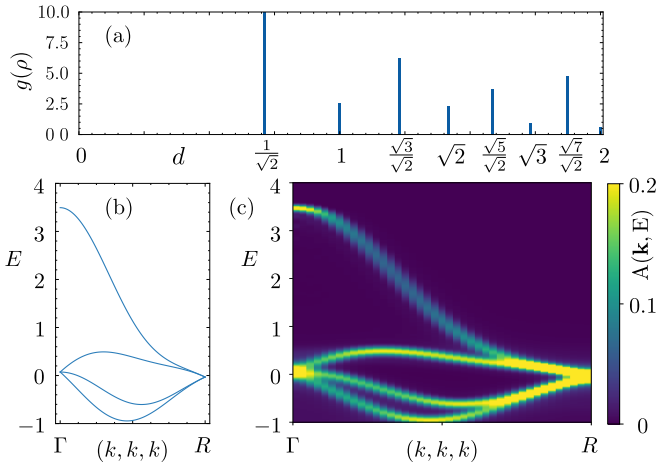

Figure S1. Panel (a) shows the radial distribution function $g(d)$ as a function of distance d for the crystalline transition metal mono-silicide. Panel (b) shows the band-structure for crystalline RhSi ($v_1 = 0.55, v_2 = 0.16$ and $v_p = -0.762$) for a cutoff distance $d_c = 1.5$ along path $\Gamma - R$ in the Brillouin zone, calculated using the Bloch Hamiltonian $\mathcal{H}$ with up to fourth-nearest neighbours. Panel (c) shows $A(\mathbf{k}, E)$ along the same path in BZ, and for the same set of parameters, calculated using the real-space Hamiltonian H.

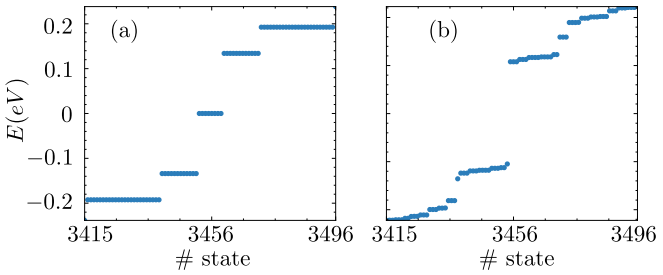

Figure S2. The low-energy spectrum of a crystalline system in parameter regime (1) with double-Weyl fermions pinned at $E = 0$ under (a) periodic boundary conditions and (b) anti-periodic boundary conditions. Both types of boundary conditions are applied in all three directions. Here, we consider a cubic system with 12^3 unit cells.

limit $\theta = 0$, this system has eight gapless states, see Fig. S2a. These states reflect the existence of two zero-energy double-Weyl fermions at the Γ and R points of the Brillouin zone. Applying anti-periodic boundary conditions (APBCs) in all directions shifts these states away from $E = 0$, as shown in Fig. S2b. This creates an energy gap that fills up with rare states once $\sigma \neq 0$.

We now study the amorphous system in regime (1), with 12^3 unit cells and with APBCs in all directions. In Fig. S3a, we plot the Hamiltonian spectrum as a function of different disorder realizations for $\sigma = 0.07$. We color all eigenstates of this spectrum according to their inverse participation ratio (IPR) $\text{IPR}_\text{n} = \sum_\text{n} \sum_\mathbf{r} |\Psi_\text{n}(\mathbf{r})|^4$, such that blue and green color indicates smaller and larger IPR, respectively. States that are shifted away from $E = 0$ have low IPR, indicating they are perturbatively

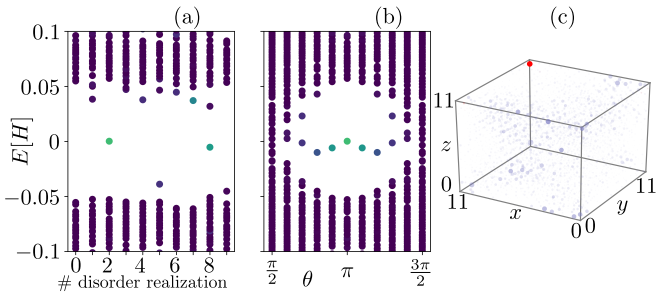

Figure S3. The low-energy spectrum of an amorphous system in parameter regime (1) under (a) anti-periodic boundary conditions and (b) twisted boundary conditions. Panel (c) shows probability density distributions several states of the amorphous system created in disorder realization $\lambda = 2$, which spectrum is shown in panel (a). Here, red color represents the low-energy state near $E = 0$, and blue color represents joint probability density distributions of three excited states lowest in energy. We assume a cubic system with 12^3 unit cells.

dressed Weyl states [4]. For disorder realizations $\lambda = 2, 8$, we observe two low-energy states with increased localization compared to the higher-energy states.

In the following, we focus on disorder realization $\lambda = 2$. The low-energy spectrum of this system as a function of twist angle θ is shown in Fig. S3b. We see that a low-energy state disperses weakly with θ compared to higher-energy states, suggesting it is a localized state [5]. Fig. S3c shows its probability density distribution (red color) at $\theta = \pi$ along with the joint probability distribution of three excited states lowest in energy (blue color). We see that the low-energy state is localized in a small region, while excited states spread over large portions of the system.

Appendix C: Semi-classical analysis of the spectral localizer

In this section, we analytically derive the low-energy spectrum of the spectral localizer for crystalline transition metal mono-silicides. This can be done using a semi-classical analysis that maps the problem of finding zero modes of the operator $\mathcal{L}$ to a well-known problem of solving for the spectrum of harmonic oscillators [6–8]. As in [6, 7], semi-classical refers to the fact that we ignore tunneling between between harmonic oscillator wells, ensured by choosing a small value of κ, as defined next.

We start with the spectral localizer introduced in Eq. (5) of the main text that is here rewritten in the following form

$$\mathcal{L} = \begin{pmatrix} \kappa D & \sigma_0 H \\ \sigma_0 H & -\kappa D \end{pmatrix}. \tag{C1}$$

Here, we are interested in bulk properties close to zero energy and thus choose $\mathbf{r} = 0$ at $E = 0$. We de-

fine $D = \sum_j \sigma_j X_j$, with X_j and H being the real-space position and Hamiltonian operators, respectively. Next, we perform a Fourier transform $\mathcal{F}$ on $\mathcal{L}$. Using $\mathcal{F}[D] = -i\sum_{j=1}^{d} \sigma_j \partial_{k_j}$ and $\mathcal{H} = \mathcal{F}[H]$, we obtain

$$\mathcal{L}_k = \begin{pmatrix} -i\kappa \sum_j \sigma_j \partial_{k_j} & \sigma_0 \mathcal{H} \\ \sigma_0 \mathcal{H} & i\kappa \sum_j \sigma_j \partial_{k_j} \end{pmatrix}. \tag{C2}$$

We study the spectral properties of the operator

$$\mathcal{L}_k^2 = \begin{pmatrix} \sigma_0(\mathcal{H}^2 - \kappa^2 \nabla_k^2) & -i\kappa \sum_{j=1}^{d} \sigma_j \partial_{k_j} \mathcal{H} \\ i\kappa \sum_{j=1}^{d} \sigma_j \partial_{k_j} \mathcal{H} & \sigma_0(\mathcal{H}^2 - \kappa^2 \nabla_k^2) \end{pmatrix} \tag{C3}$$

that is, by construction, non-negative and, as will be shown shortly, has harmonic potential wells at Weyl points [6].

1. Parameter regime (1)

To build intuition we focus on crystalline systems in parameter regime (1) with nonzero hoppings v_p. To simplify our analysis, we consider the case with cutoff radius $d_c = 1.01$ such that only nearest-neighbors are related by nonzero hoppings. From Eq. (A2), we get

$$\mathcal{H} = v_p[\gamma_y \delta_z \cos\frac{k_x}{2} \sin\frac{k_y}{2} + \gamma_y \delta_x \cos\frac{k_y}{2} \sin\frac{k_z}{2} + \gamma_0 \delta_y \cos\frac{k_z}{2} \sin\frac{k_x}{2}]. \tag{C4}$$

We are interested in the low-energy counterpart of this Hamiltonian in order to study the low-energy spectrum of $\mathcal{L}_k^2$. To probe a double-Weyl fermion at the Γ point, we expand $\mathcal{H}$ close to $\mathbf{k} = 0$ to first order in $\mathbf{k}$ and obtain

$$\mathcal{H} = v_p[\gamma_0 \delta_y \frac{k_x}{2} + \gamma_y \delta_z \frac{k_y}{2} + \gamma_y \delta_x \frac{k_z}{2}]. \tag{C5}$$

We can bring this Hamiltonian into a block-diagonal form characteristic for double-Weyl fermions [9], by performing a unitary transformation $U\mathcal{H}U^\dagger$ with $U = \frac{1}{\sqrt{2}}(\gamma_0 - i\gamma_x)\delta_0$ and redefining momenta as $k_x \to k_y \to k_z \to k_x$. This results in

$$\mathcal{H} = \frac{v_p}{2}[\gamma_z \delta_x k_x + \gamma_0 \delta_y k_y + \gamma_z \delta_z k_z]. \tag{C6}$$

From here, we readily obtain the operator $\mathcal{L}_k^2$ as

$$\mathcal{L}_k^2 = \begin{pmatrix} \sigma_0\gamma_0\delta_0[\frac{v_p^2}{4}(k_x^2 + k_y^2 + k_z^2) - \kappa^2\nabla_k^2] & -i\frac{v_p\kappa}{2}(\sigma_x\gamma_z\delta_x + \sigma_y\gamma_0\delta_y + \sigma_z\gamma_z\delta_z) \\ i\frac{v_p\kappa}{2}(\sigma_x\gamma_z\delta_x + \sigma_y\gamma_0\delta_y + \sigma_z\gamma_z\delta_z) & \sigma_0\gamma_0\delta_0[\frac{v_p^2}{4}(k_x^2 + k_y^2 + k_z^2) - \kappa^2\nabla_k^2] \end{pmatrix}. \tag{C7}$$

We observe that the diagonal elements $[-\kappa^2\nabla_k^2 + \frac{v_p^2}{4}(k_x^2 + k_y^2 + k_z^2)]$ describe the equation of a 3D quantum harmonic oscillator in momentum space upon identifying $\hbar = \kappa, m = \frac{1}{2}$ and $\omega = v_p$. The eigenvalues of this harmonic oscillator are $\epsilon_n^{\mathrm{d}} = \hbar\omega(n + \frac{3}{2}) = \kappa v_p(n + \frac{3}{2})$ where $n \in \mathbb{N}$. The lowest energy $\epsilon_0^{\mathrm{d}} = \frac{3v_p\kappa}{2}$ is obtained for $n = 0$. Note that these eigenvalues are sixteen-fold degenerate because they originate from the diagonal part of $\mathcal{L}_k^2$.

The eigenvalues of the off-diagonal part can be obtained by its diagonalization. The sixteen eigenvalues consists of doubly degenerate $\pm\frac{3v_p\kappa}{2}$ and sixfold degenerate $\pm\frac{v_p\kappa}{2}$. Thus, because diagonal and off-diagonal parts of operator $\mathcal{L}_k^2$ commute, its spectrum can be obtained by simply summing their respective eigenvalues, i.e., $\epsilon_n = \epsilon_n^{\mathrm{d}} + \epsilon^{\mathrm{off-d}}$. For $n = 0$, we see that the doubly degenerate $\epsilon^{\mathrm{off-d}} = -\frac{3v_p\kappa}{2}$ exactly cancels out the diagonal contribution $\epsilon_0^{\mathrm{d}} = \frac{3v_p\kappa}{2}$, resulting in two zero modes for the operator $\mathcal{L}_k^2$. Thus, we obtain that a single double-Weyl fermion at Γ point yields two zero modes of operator $\mathcal{L}_k^2$, and via the inverse Fourier transformation, also for the operator $\mathcal{L}^2$. Similarly, the double-Weyl fermion at R point also contributes two zero modes of the operators $\mathcal{L}_k^2$, and $\mathcal{L}$. Hence, we can predict analytically that the operator $\mathcal{L}$ will have four zero modes for crystalline systems described by the Hamiltonian Eq. (C4).

The presence of longer range hoppings, such as the third nearest neighbor hoppings does not alter this conclusion. This is because such hopping terms, given by Eq. (A5), have the same matrix structure as the Hamiltonian Eq. (C4). Hence, when expanding up to linear order in k, the matrix structure remains the same as for the Hamiltonian Eq. (C5), and the only difference is in the prefactors. Thus, longer range hoppings with amplitudes proportional v_p can only alter states higher in the spectrum of $\mathcal{L}$.

We confirm this analytical prediction numerically for

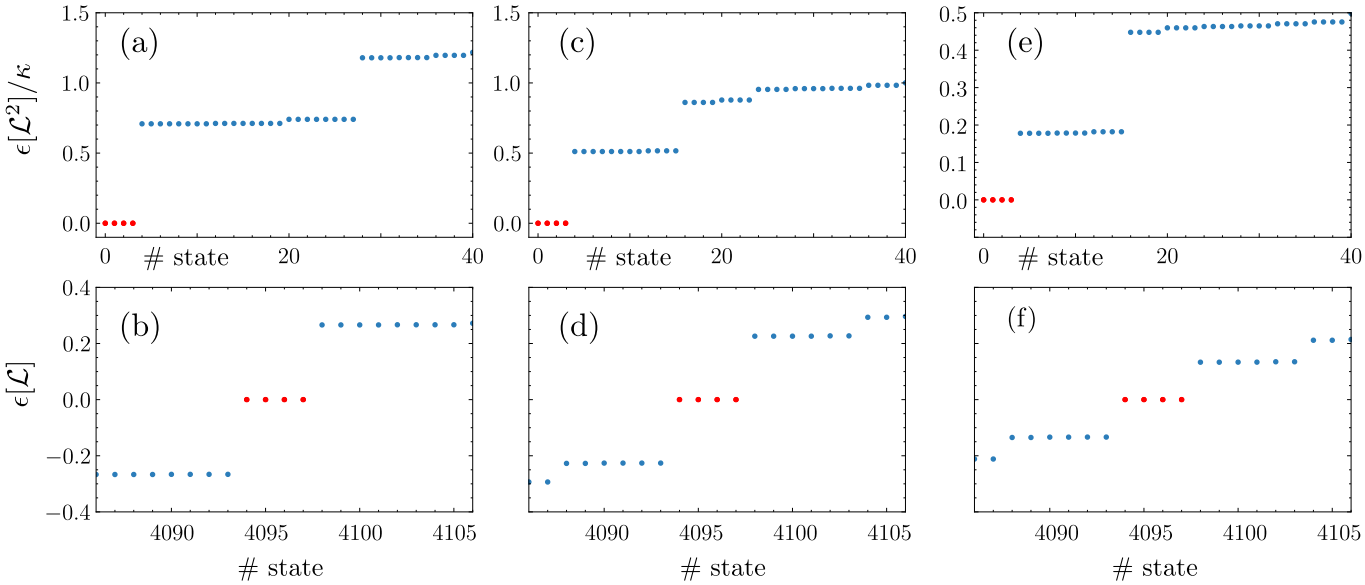

Figure S4. Panels (a, c, e) and (b, d, f) show the spectra of the operators $\mathcal{L}^2$ and $\mathcal{L}$, respectively. These operators are calculated for $\kappa = 0.1$ and a crystalline system of linear size $L = 8$. Panels (a, b) and (c, d) consider parameter regime (1) and has $d_c 1.01$ and $d_c = 1.5$, respectively. Panels (e,f), consider parameter regime (2) with $d_c = 1.01$. We use hopping amplitudes $v_p = -0.762$ and $v_2 - 0.16$. Red and blue color represents zero modes and excited states, respectively.

$v_p = -0.762$. Figs. S4a and b show the spectrum of operators $\mathcal{L}^2$ and $\mathcal{L}$, respectively for the system with linear size $L = 8$ and $\kappa = 0.1$ in case of nonzero nearest-neighbor hoppings. Furthermore, we obtain similar spectra once the third-nearest-neighbor hoppings are included, see Figs. S4c, d. We see that adding more hoppings preserves the existence of four degenerate zero modes but reduces the gap between them and states at higher energy.

2. Parameter regime (2)

Next, we study how including hoppings with amplitudes v_1, v_2 affect the spectrum of the operator $\mathcal{L}$. For simplicity, we assume that only nearest-neighbor and second-nearest-neighbor hoppings are present. In parameter regime (2), the crystalline system hosts a threefold fermion at the Γ point and a double-Weyl fermion at the R point. Since we derived the low-lying localizer spectrum for a double-Weyl in the previous section, here we focus on the Γ point. Close to Γ, the low-energy Hamiltonian reads

$$\mathcal{H} = 3v_2\gamma_0\delta_0 + v_1[\gamma_x\delta_0 + \gamma_x\delta_x + \gamma_0\delta_x] + \frac{v_p}{2}[\gamma_y\delta_z k_y + \gamma_y\delta_x k_z + \gamma_0\delta_y k_x]. \tag{C8}$$

As before, we perform the unitary transformation on $\mathcal{H}$ with $U = \frac{1}{\sqrt{2}}(\gamma_0 - i\gamma_x)\delta_0$ and exchange momenta as $k_x \to k_y \to k_z \to k_x$. This yields

$$\mathcal{H} = 3v_2\gamma_0\delta_0 + v_1[\gamma_x\delta_0 + \gamma_x\delta_x + \gamma_0\delta_x] + \frac{v_p}{2}[\gamma_z\delta_x k_x + \gamma_0\delta_y k_y + \gamma_z\delta_z k_z]. \tag{C9}$$

After squaring this Hamiltonian, we perform a unitary transformation $U\mathcal{H}^2U^\dagger = \tilde{\mathcal{H}}^2$ with $U = \frac{1}{\sqrt{2}}(\gamma_0 - i\gamma_x)\delta_0$ to write it in the following form

$$\begin{aligned}\tilde{\mathcal{H}}^2 =&[3v_1^2 + 9v_2^2 + \frac{v_p^2}{4}(k_x^2 + k_y^2 + k_z^2)]\gamma_0\delta_0 + (2v_1^2 + 6v_1v_2)[\gamma_x\delta_0 + \gamma_x\delta_x + \gamma_0\delta_x] + \\ &v_1v_p[k_z\gamma_z\delta_y - k_x\gamma_y\delta_0 + k_y\gamma_x\delta_y] + 3v_2v_p[k_y\gamma_0\delta_y - k_x\gamma_y\sigma_x - k_z\gamma_y\sigma_z].\end{aligned} \tag{C10}$$

In the eigenbasis, the matrix $\tilde{\mathcal{H}}^2$ has eigenvalues

$$3v_1^2 + 9v_2^2 + \frac{v_p^2}{4}(k_x^2 + k_y^2 + k_z^2) - 2v_1(v_1 + 3v_2) \pm v_p(v_1 - 3v_2)\sqrt{k_x^2 + k_y^2 + k_z^2}, \tag{C11}$$

and

$$3v_1^2+9v_2^2+\frac{v_p^2}{4}(k_x^2+k_y^2+k_z^2)+2v_1(v_1+3v_2)\pm(v_1+3v_2)\sqrt{16v_1^2+v_p^2(k_x^2+k_y^2+k_z^2)}. \tag{C12}$$

Following Eq. (C3), the diagonal elements of $\tilde{\mathcal{H}}^2$, written in the eigenbasis, become part of the diagonal elements of $\mathcal{L}_k^2$. We focus first on Eq. (C11) of of matrix $\tilde{\mathcal{H}}^2$ which leads to the diagonal entries

$$-\kappa^2\nabla_k^2+\frac{v_p^2}{4}(k_x^2+k_y^2+k_z^2)\pm v_p(v_1-3v_2)\sqrt{k_x^2+k_y^2+k_z^2}+3v_1^2+9v_2^2-2v_1(v_1+3v_2) \tag{C13}$$

of $\mathcal{L}_k^2$. Upon identifying $\kappa=\hbar, m=\frac{1}{2}$ and $\omega=v_p$, we recognize Eq. (C13) as the Hamiltonian of a 3D quantum harmonic oscillator under a constant force and with a constant energy offset. Using the spherical coordinates ($k_x=k\cos\theta\sin\phi, k_y=k\cos\theta\cos\phi$ and $k_z=k\sin\theta$), we obtain

$$H_{\text{h.o.}}=-\kappa^2\nabla_k^2+\frac{v_p^2}{4}k^2\pm v_p(v_1-3v_2)k+v_1^2+9v_2^2-6v_1v_2, \tag{C14}$$

and by completing the square in k, Eq. (C14) becomes

$$H_{\text{h.o.}}=-\kappa^2\nabla_k^2+\frac{v_p^2}{4}\left(k\pm\frac{2(v_1-3v_2)}{v_p}\right)^2. \tag{C15}$$

Upon replacing $\kappa^2\to\frac{\hbar^2}{2m}, \frac{v_p^2}{4}\to\frac{m\omega^2}{2}, k'=k\pm\frac{2(v_1-3v_2)}{v_p}$ and $\nabla_k^2\to\nabla_{k'}^2$, we recognize an equation of a 3D quantum harmonic oscillator in spherical coordinates. Hence, for each diagonal element Eq. (C11) of matrix $\tilde{\mathcal{H}}^2$, we obtain that matrix $\mathcal{L}_k^2$ has eigenvalues $\epsilon_n^{\text{d},1}=\tau_0\sigma_0\kappa v_p(n+\frac{3}{2})$.

We are left to calculate the diagonal elements of $\mathcal{L}_k^2$ corresponding to Eq. (C12), which read

$$-\kappa^2\nabla_k^2+\frac{v_p^2}{4}(k_x^2+k_y^2+k_z^2)+3v_1^2+9v_2^2+2v_1(v_1+3v_2)\pm(v_1+3v_2)\sqrt{16v_1^2+v_p^2(k_x^2+k_y^2+k_z^2)}. \tag{C16}$$

In this case we are not able to find an general analytical expression, and so we resort to first-order perturbation theory in v_1, v_2 to determine the corresponding ground state energies. For this, we separate two unperturbed $H_{\text{h.o.}}=-\kappa^2\nabla_k^2+\frac{v_p^2}{4}(k_x^2+k_y^2+k_z^2)$ and the perturbation term $H_{\text{p}}^{\pm}=3v_1^2+9v_2^2+2v_1(v_1+3v_2)\pm(v_1+3v_2)\sqrt{16v_1^2+v_p^2(k_x^2+k_y^2+k_z^2)}$, which contains all terms proportional to v_1, v_2. In spherical coordinates, $H_{\text{h.o.}}=-\kappa^2\nabla_k^2+\frac{v_p^2}{4}k^2$ and $H_{\text{p}}^{\pm}=3v_1^2+9v_2^2+2v_1(v_1+3v_2)\pm(v_1+3v_2)\sqrt{16v_1^2+v_p^2k^2}$. The ground state energy of $H_{\text{h.o.}}$ is $\frac{3\kappa v_p}{2}$ and the corresponding wave-function is $\Psi_{GS}(\mathbf{k})=(\beta^2/\pi)^{3/4}\exp\left[-\beta^2k^2/2\right]$ where $\beta=\sqrt{v_p/2\kappa}$. In the first approximation, $H_{\text{p}}^{\pm}$ contributes with the energy $E_{\text{p}}^{\pm}=4\pi\int_0^{\infty}\Psi_{GS}^*(\mathbf{k})H_{\text{h.o.}}\Psi_{GS}(\mathbf{k})k^2dk$. Here, we have already used the fact that $H_{\text{h.o.}}$ is a spherically symmetric function such that the angular dependence is already integrated out. We solve this integral numerically. To simplify the analysis, we assume that parameters v_1 and v_2 are not independent. In particular $v_2=v_1/\chi$ where $\chi=3.4375$ is chosen such that it reflects the ratios of amplitudes v_1 and v_2 for crystalline RhSi. In Fig. S5, we plot the perturbed eigenvalues $\epsilon_0^{\text{d},2\pm}=\frac{3\kappa v_p}{2}+E_{\text{p}}^{\pm}$ as a function of parameter v_1. We see that H_{p}^{+} monotonously increases the ground state energy while H_{p}^{-} mildly reduces it for $v_1\lessapprox 1.9$.

Lastly, we evaluate the eigenvalues of the off-diagonal block of operator $\mathcal{L}_k^2$. From Eqs. (C3) and (C9), we obtain

$$\kappa\sum_{j=1}^{d}\sigma_j\partial_{k_j}\mathcal{H}=\frac{v_p\kappa}{2}(\sigma_x\gamma_z\delta_x+\sigma_y\gamma_0\delta_y+\sigma_z\gamma_z\delta_z). \tag{C17}$$

The eigenvalues of this off-diagonal part are not changed upon subsequent unitary rotations used to obtain matrix $\tilde{\mathcal{H}}$ and bring it into the eigenbasis. They consist of doubly degenerate $\epsilon^{\text{off-d},1\pm}=\pm\frac{3v_p\kappa}{2}$ and six-fold degenerate $\epsilon^{\text{off-d},2\pm}=\pm\frac{v_p\kappa}{2}$.

Finally, we can determine the ground state energy of operator $\mathcal{L}_k^2$. As before, it is a sum of diagonal and off-diagonal contributions. Since the maximal amplitude of off-diagonal contributions is $\frac{3v_p\kappa}{2}$, we focus on

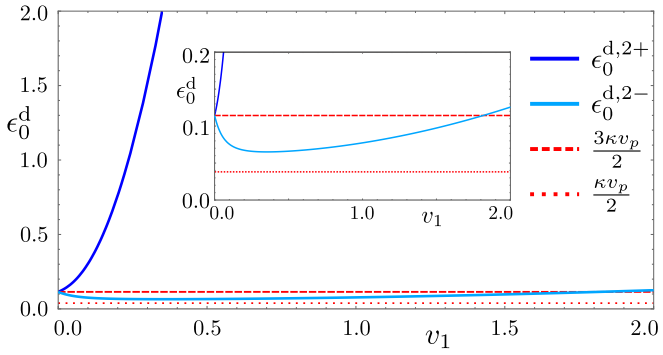

Figure S5. Ground state energy for the Hamiltonians Eq. (C16) as function of v_1. This energy is determined using first-order perturbation theory. Dashed and dotted lines represent positive eigenvalues of the matrix Eq. (C17).

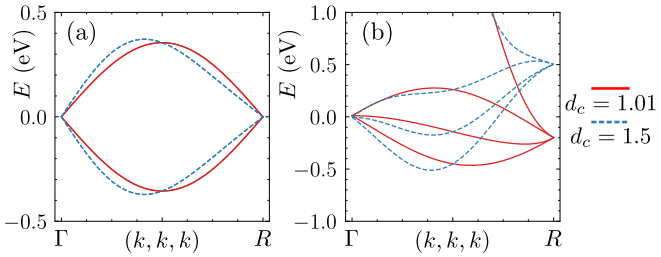

Figure S6. The band-structure of crystalline CoSi in parameter regimes (1) and (2) is shown in panels (a) and (b), respectively. Red curves show the spectrum for cutoff distance $d_c = 1.01$, while blue curves show the spectrum once $d_c = 1.5$.

$n = 0$ limit for the diagonal contributions. These are eight-fold degenerate $\epsilon_0^{\rm d,1} = \frac{3\kappa v_p}{2}$ and four-fold degenerate $\epsilon_0^{\rm d,2\pm} = \frac{3\kappa v_p}{2} + E_{\rm p}^{\pm}$ plotted in Fig. S5. Clearly, $\epsilon_0^{\rm d,1} + \epsilon^{\rm off-d,1-} = 0$ and is doubly degenerate because $\epsilon^{\rm off-d,1\pm}$ is doubly degenerate. Moreover, $\epsilon_0^{\rm d,1} + \epsilon_0^{\rm off-d,2\pm}$ is always nonzero. Regarding $\epsilon^{\rm d,2\pm}$, $\epsilon^{\rm d,2\pm} + \epsilon^{\rm off-d,1-} = E_{\rm p}^{\pm}$ that is nonzero $0 < v_1 < 1.5$ as shown in Fig. S5. This range of values covers the parameter regimes of RhSi and CoSi. From Fig. S5, we see that $\epsilon^{\rm d,2\pm}$ never crosses any off-diagonal contribution $\epsilon^{\rm off-d,1\pm}/\epsilon^{\rm off-d,2\pm}$ that is represented with dashed/dotted horizontal red lines. Thus, for $0 < v_1 < 1.5$ these diagonal terms can never produce zero states of operator $\mathcal{L}_k^2$. We conclude that the operator $\mathcal{L}_k^2$ has two zero modes for a threefold fermion of monopole charge $C = 2$ in case of RhSi/CoSi. Due to a double-Weyl fermion at the R point, $\mathcal{L}_k^2$ will have four zero states in total for parameter regime (2). This semi-analytical result is confirmed upon diagonalizing the full real space operators $\mathcal{L}^2$ and $\mathcal{L}$ for parameters $v_1 = 0.55, v_2 = 0.16, v_p = -0.762$, see Fig. S4e, f.

In numerics, we observe that increasing values of κ reduces the range of v_1, v_2 values for which our analytical prediction holds. This is consistent with the expectation stemming from a more rigorous analysis of the eigenvalues of operator $\mathcal{L}_k^2$ in Eq. (C3), where κ is necessarily assumed to be a small quantity [6, 7]. Indeed, for large values of κ, we cannot ignore the tunnel effect between two harmonic wells that increases the energies of states within these wells [6]. Hence, the analysis in this section is usually referred to as semi-classical [6, 7].

In addition, for smaller values of $\kappa \sim 0.1$, we obtain that increasing v_1, v_2 also leads to the breakdown of the semi-classical analysis. Such a behavior is expected because nonzero v_1, v_2 produce multifold fermions at Γ and R points at different energies. The energy difference in fact increases with larger v_1, v_2, implying that the spectral localizer calculated at $E = 0$ is not anymore capturing only the low-energy physics of the problem. The spectrum of operator $\mathcal{L}$ in this case can be derived by mapping it to the Dirac equation [8].

Appendix D: Results for CoSi

In the main text, we have analyzed how amorphicity affects RhSi using different quantities such as the density of states, adjacent level spacing ratio and spectral localizer. In this section, we repeat those calculations for parameters chose to model a-CoSi.

Like in the main text, we consider two parameter regimes. In regime (1), parameters read $v_1 = v_2 = 0$ and $v_p = 0.41$. The regime (2) has parameters $\mu = 0.551, v_1 = 1.29, v_2 = 0.25$ and $v_p = 0.41$, where μ is the chemical potential represented by $\mathcal{H}_0 = \mu\gamma_0\delta_0$. Here, all parameters are given in units of eV. Since parameter regime (2) reproduces well the band-structure of crystalline CoSi at the Fermi level [10], we shall often refer to it as the a-CoSi regime in the following.

The resulting band-structures for regimes (1) and (2) are shown in Figs. S6a and b, respectively. Here, solid red lines represent the band-structure corresponding to the Hamiltonian $\mathcal{H}_0 + \mathcal{H}_1 + \mathcal{H}_2$. Dashed blue lines indicate the band-structure for a cutoff distance $d_c = 1.5$ that corresponds to studying the Hamiltonian $\mathcal{H}_0 + \mathcal{H}_1 + \mathcal{H}_2 + \mathcal{H}_3 + \mathcal{H}_4$. We see that the spectrum of CoSi in regime (1) along the $\Gamma - R$ path looks very similar to the corresponding spectrum of RhSi shown in Fig. 1c of the main text, in the sense that the threefold fermion is placed at higher energy compared to the double-Weyl fermion. This is not anymore the case for regime (2), as we see that longer range hoppings lift the double-Weyl fermion higher in energy compared to the threefold fermion, unlike the situation in RhSi. Lastly, we see that bands along the $\Gamma - R$ path disperse less in CoSi than in RhSi.

1. Spectral properties

Having fewer dispersive bands greatly affects spectral properties of a-CoSi, as it allows disorder to couple states at different energies with smaller energy penalty. Fig. S7a

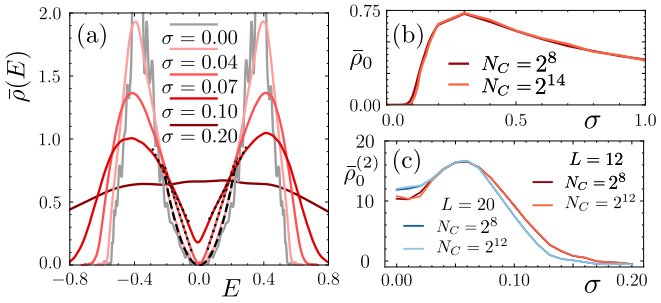

Figure S7. Panel (a) shows how $\bar{\rho}(E)$ vs E changes with σ. Dashed and dotted lines represent fit functions αE^2 and $\alpha + \beta|E|$, respectively. Panel (b) shows how zero-energy averaged DOS $\bar{\rho}_0$ changes with σ. Panel (c) shows $\bar{\rho}_0^{(2)}$ as a function of disorder strength. We define $\bar{\rho}^{(2)}(0) = \sum_{\lambda=1}^{N_{\rm dis}} (\rho^\lambda)^{(2)}(0)$ where $(\rho^\lambda)^{(2)}(0)$ is estimated from a fit $\rho^\lambda(E) = \rho_0^\lambda + (\rho^\lambda)^{(2)}(0)E^2$ in the energy range $(-0.2, 0.2)$ for independent disorder realizations λ.

shows the averaged density of states for a-CoSi in parameter regime (1). We immediately observe that $\bar{\rho}(E)$ for a crystalline system reaches its maximal values for approximately two times smaller energies compared to a-RhSi, see also Fig. 2a of the main text. For small values of disorder ($\sigma \approx 0.04$) $\bar{\rho}(E) \propto E^2$, characteristic for linearly dispersing bands. As disorder strength is increased to $\sigma \approx 0.07$, a behavior $\bar{\rho}(E) \propto |E|$ emerges that is characteristic of the proximity of the quantum critical point. This behavior persists for $\sigma = 0.1$, along with nonzero DOS at zero energy . Finally, stronger disorder strengths yield broad and featureless DOS characteristic for diffusive metals. In Fig. S7b, we plot $\bar{\rho}_0$ as a function of disorder strength, and see it becomes nonzero for $\sigma \lessapprox 0.1$.

To study the semimetal-diffusive metal phase transition, we plot in Fig. S7c the second derivative $\bar{\rho}_0^{(2)}$ as a function of disorder for different system sizes and orders N_C of the KPM expansion. This quantity peaks at $\sigma_c \approx 0.06$ signaling the proximity of the quantum critical point. It however does not diverge with varying parameters, implying that the phase transition between semimetal and diffusive metal regimes is avoided, just like for a-RhSi in parameter regime (1).

2. Anderson localization

To study localization properties of a-CoSi, we use the adjacent level spacing ratio $\bar{r}$ (Eq. (4) of the main text) and the inverse participation ratio $\overline{\rm IPR}$ at the Fermi level. The results for two parameter regimes are shown in Fig. S8. From Fig. S8a, we see that the system in regime (1) is a diffusive metal for $\sigma < \sigma_l \approx 0.8$, and an Anderson insulator for $\sigma > \sigma_{\rm AI} \approx 3.6$ with a gradual transition for σ values in between. In the a-CoSi regime, we see from Fig. S8b that the diffusive metal phase persists to much larger disorder strengths, namely

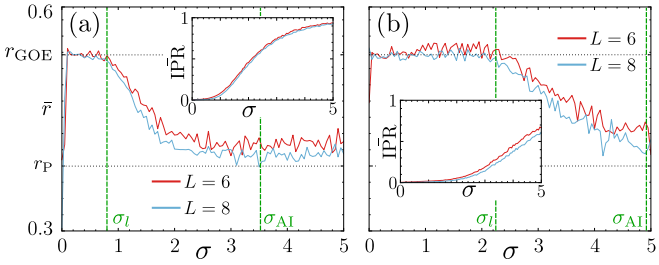

Figure S8. Panels (a) and (b) show adjacent level spacing ratios at $E_F = 0$ as a function of disorder strength σ for parameter regimes (1) and (2), respectively. Here, $r_{\rm GOE} = 0.536$ and $r_{\rm P} = 0.387$ are represented by dotted gray lines, while dashed green lines represent disorder strengths σ_l and $\sigma_{\rm AI}$ The insets show how the corresponding inverse participation ratios at the Fermi energy evolve with σ.

up to $\sigma_l \approx 2.2$. This can be expected because of larger hopping amplitudes in regime (2), that counteract the effects of disorder induced localization of eigenstates. The system experiences a gradual transition to the Anderson insulator regime that is reached for $\sigma_{\rm AI} \approx 5$.

3. Topological phase diagram

Lastly, we review the topological phase diagram of a-CoSi. The results are shown in Fig. S9. To produce this figure, we used $N_{\rm dis} = 25$ disorder realizations and cubic systems of linear size $L = 12$ unit cells.

For parameter regime (1), we observe that the topological phase diagram shown in Figs. S9a,b looks very similar to the phase diagrams calculated for a-RhSi in both regimes. The gap between pairs of midgap modes and excited states in Fig. S9a closes at $\sigma_{\rm TDM} \approx 0.2$. In addition, we observe from the inset of Fig. S9b that for low disorder strengths $\sigma \leq 0.1$, the averaged energy $\bar{\epsilon}_0$ of the $\mathcal{L}$ midgap mode follows the analytically predicted behavior $\bar{\epsilon}_0 = \sigma^{3/4}\kappa$ [7]. We also find that the dependence of $\bar{\epsilon}_0$ on σ can be well approximated in the entire range $\sigma \in [0, 2.5]$ by an $a\sqrt{\sigma}$ law, where $a = 0.077$.

In a-CoSi regime, the phase diagram in Fig. S9c reveals that the topological properties of a-CoSi are less robust to effects of disorder compared to a-RhSi. The gap between midgap and first excited states of $\mathcal{L}$ operator closes at $\sigma_{\rm TDM} \approx 0.075$, while in a-RhSi it closes for $\sigma_{\rm TDM} \approx 0.25$. Moreover, In the limit $\sigma = 0$, this gap is approximately two times smaller than the corresponding gap in regime (1) of the same material. Disorder averaged eigenvalues $\bar{\epsilon}_0, \bar{\epsilon}_1$ shown in Fig. S9d reveal that $\bar{\epsilon}_0$ is well approximated by $a\sqrt{\sigma}$ ($a = 0.073$) only for $\sigma > 0.5$. The inset of Fig. S9d shows $\bar{\epsilon}_0, \bar{\epsilon}_1$ for very small disorder strengths. We see that $\bar{\epsilon}_1$ experiences an upturn at $\sigma \approx 0.075$, while $\bar{\epsilon}_0$ cannot be well approximated with the analytical prediction $\bar{\epsilon}_0 = \sigma^{3/4}\kappa$, where $\kappa = 0.1$.

As mentioned in the main text, we relate this reduced topological robustness of a-CoSi compared to a-RhSi,

to different ratios of inter-orbital hoppings for the two cases. As shown in Fig. 1 of the main text, there are two types of inter-orbital hoppings v_1 and v_p. The latter one changes with the bond orientation, such that the hoppings $\frac{1}{4}(v_1 \pm v_p)$ are arranged into the chiral structure resulting in the appearance of multifold fermions in parameter regime (2). In the presence of structural disorder that alters hoppings between orbitals, this chiral structure is gradually lost as σ is increased. Thus, the relevant energy scale at which disorder effects alter topology is proportional to $\Delta v_{\mathrm{nn}} = \frac{v_p}{2} = \frac{1}{4}(v_1 + v_p) - \frac{1}{4}(v_1 - v_p)$.

In crystalline RhSi, $v_1 = 0.55$ and $v_p = -0.762$ such that the nearest-neighbor hoppings have amplitudes $\frac{1}{4}(v_1 + v_p) = -0.053$ and $\frac{1}{4}(v_1 - v_p) = 0.328$, and they differ by $|\Delta v_{\mathrm{nn}}| = \frac{|v_2|}{2} = 0.381$. For crystalline CoSi, parameters read $v_1 = 1.29$ and $v_p = 0.41$ implying that $\frac{1}{4}(v_1 + v_p) = 0.425$, $\frac{1}{4}(v_1 - v_p) = 0.22$ and their difference reads $|\Delta v_{\mathrm{nn}}| = 0.205$. Thus, we conclude that the disorder strength at which the topological phase transition occurs is approximately two times smaller for a-CoSi than for a-RhSi, and this is indeed observed in numerical analysis using the spectral localizer.

Finally, in Table (D 3), we summarize all critical disorder strengths determined in this work for a-RhSi and a-CoSi in regime (2). Note that the amorphous system is always in the diffusive metal phase.

quantities	a-RhSi	a-CoSi
$\lvert\Delta v_{\mathrm{nn}}\rvert$	0.328	0.205
σ_{TDM}	0.3	0.07
σ_l	1.7	2.2
σ_{AI}	4.6	5

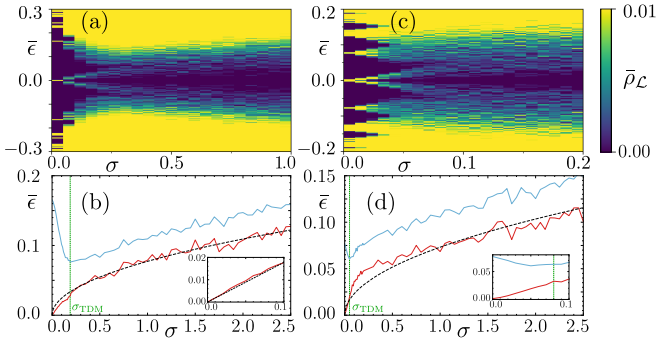

Figure S9. Panels (a) and (b) show disorder-averaged DOS of the operator $\mathcal{L}$ as a function of disorder strength σ for parameter regimes (1) and (2), respectively. In panels (c) and (d) are plotted disorder averaged energies of midgap and first-excited states $\bar{\epsilon}_0, \bar{\epsilon}_1$ as a function of σ for these two parameter regimes. Here, dashed green lines represent the topological phase transition point σ_{TDM}. Dashed black lines represents a fit $\bar{\epsilon}_0 = a\sqrt{\sigma}$, where $a = 0.077$ in regime (1) and $a = 0.073$ for regime (2). The inset of panels (b) and (d) show how well $\bar{\epsilon}_0$ matches with the predicted form $\kappa^{0.75}\sigma$ [7] (gray line) in case of small disorder strengths. Here, we use $\kappa = 0.1, \mathrm{N}_{\mathrm{dis}} = 25$ and $L = 12$.

[1] G. Chang, S.-Y. Xu, B. J. Wieder, D. S. Sanchez, S.-M. Huang, I. Belopolski, T.-R. Chang, S. Zhang, A. Bansil, H. Lin, and M. Z. Hasan, Unconventional chiral fermions and large topological Fermi arcs in RhSi, Phys. Rev. Lett. **119**, 206401 (2017).

[2] Q. Marsal, *Topological phases in amorphous matter* (Universite Grenoble Alpes, 2023).

[3] J. H. Pixley, D. A. Huse, and S. Das Sarma, Rare-region-induced avoided quantum criticality in disordered three-dimensional Dirac and Weyl semimetals, Phys. Rev. X **6**, 021042 (2016).

[4] J. Pixley and J. H. Wilson, Rare regions and avoided quantum criticality in disordered Weyl semimetals and superconductors, Annals of Physics **435**, 168455 (2021).

[5] J. H. Pixley, P. Goswami, and S. Das Sarma, Anderson localization and the quantum phase diagram of three dimensional disordered Dirac semimetals, Phys. Rev. Lett. **115**, 076601 (2015).

[6] H. Schulz-Baldes and T. Stoiber, Invariants of disordered semimetals via the spectral localizer, Europhysics Letters **136**, 27001 (2022).

[7] H. Schulz-Baldes and T. Stoiber, Spectral localization for semimetals and Callias operators, Preprint at https://arxiv.org/abs/2203.15014 (2022).

[8] S. Franca and A. G. Grushin, Obstructions in trivial metals as topological insulator zero-modes, Preprint at https://arxiv.org/abs/2304.01983 (2023).

[9] B. Bradlyn, J. Cano, Z. Wang, M. G. Vergniory, C. Felser, R. J. Cava, and B. A. Bernevig, Beyond Dirac and Weyl fermions: Unconventional quasiparticles in conventional crystals, Science **353**, aaf5037 (2016).

[10] B. Xu, Z. Fang, M. Ángel Sánchez-Martínez, J. W. F. Venderbos, Z. Ni, T. Qiu, K. Manna, K. Wang, J. Paglione, C. Bernhard, C. Felser, E. J. Mele, A. G. Grushin, A. M. Rappe, and L. Wu, Optical signatures of multifold fermions in the chiral topological semimetal CoSi, Proceedings of the National Academy of Sciences **117**, 27104 (2020).